Journal of The Electrochemical Society

The Electrochemical Society
Advancing solid state & electrochemical science & technology

OPEN ACCESS

Nitrogen Plasma Modified Carbons for PEMFC with Increased Interaction with Catalyst and Ionomer

To cite this article: Alice Parnière *et al* 2022 *J. Electrochem. Soc.* **169** 044502

View the article online for updates and enhancements.

Investigate your battery materials under defined force!
The new PAT-Cell-Force, especially suitable for solid-state electrolytes!

- Battery test cell for force adjustment and measurement, 0 to 1500 Newton (0-5.9 MPa at 18mm electrode diameter)
- Additional monitoring of gas pressure and temperature

www.el-cell.com +49 (0) 40 79012 737 sales@el-cell.com

EL-CELL®
electrochemical test equipment

This content was downloaded from IP address 194.57.116.220 on 22/06/2022 at 15:30

Journal of The Electrochemical Society, 2022 **169** 044502

Nitrogen Plasma Modified Carbons for PEMFC with Increased Interaction with Catalyst and Ionomer

Alice Parnière,[1] Pierre-Yves Blanchard,[1,z] Sara Cavaliere,[1,2,z] Nicolas Donzel,[1] Bénédicte Prelot,[1] Jacques Rozière,[1,*] and Deborah J. Jones[1,]**

[1]*ICGM, University of Montpellier, CNRS, ENSCM, 34095 Montpellier Cedex 5, France*
[2]*Institut Universitaire de France (IUF), 75231 Paris Cedex 5, France*

Vulcan XC72 carbon black, conventionally used as electrocatalyst support in proton exchange membrane fuel cells, was doped with nitrogen functionalities by exposing it to nitrogen plasma, and the effect on its morphology, structure and texture and surface properties was investigated. In particular, the strength of the interaction between the modified carbon and Nafion® ionomer was evaluated by isothermal titration calorimetry, and an enhanced exothermic effect was observed on increasing the amount of nitrogen at the Vulcan surface. The undoped and nitrogen-doped carbon blacks were catalysed with Pt nanoparticles, and the resulting materials were characterised for their electrocatalytic properties towards the oxygen reduction reaction. The electrocatalyst using nitrogen-doped supports are characterised by higher activity and stability, which is attributed to a strong Pt-support interaction promoted by the presence of the heteroatoms.
© 2022 The Author(s). Published on behalf of The Electrochemical Society by IOP Publishing Limited. This is an open access article distributed under the terms of the Creative Commons Attribution 4.0 License (CC BY, http://creativecommons.org/licenses/by/4.0/), which permits unrestricted reuse of the work in any medium, provided the original work is properly cited. [DOI: 10.1149/1945-7111/ac609e]

Manuscript submitted November 15, 2021; revised manuscript received March 9, 2022. Published April 4, 2022. *This paper is part of the JES Focus Issue on Women in Electrochemistry.*

Supplementary material for this article is available online

To meet activity, durability and cost requirements necessary for the widespread adoption of proton exchange membrane fuel cells (PEMFC), novel materials comprising membrane electrode assemblies (MEAs) are being investigated extensively. In particular, highly durable and active electrocatalysts bearing the minimum loading of platinum are needed at the cathode, where the oxygen reduction reaction (ORR) occurs. The approaches to achieving high ORR activity and to mitigating electrode degradation address both the development of architectured (multi-)metal catalysts[1,2] and of tailored support materials.[3] The latter are conventionally carbon blacks, which fulfil the main requirements of high electrical conductivity to facilitate electron transport and high surface area to disperse both the electrocatalyst, for its maximum exploitation, and the ionomer, for high proton conductivity and oxygen permeability. However, carbon blacks present two main shortcomings, related to the poor attachment of Pt nanocatalysts to their surface and the lack of stability at the high potential excursions occurring in start/stop events on automotive operation.[4] A wide range of carbon materials has been investigated as Pt supports, including graphitised carbon blacks, graphene, carbon nanotubes, carbon nanofibres, carbon aerogels and porous carbon microspheres[5–10] with the possibility of increasing their degree of graphitisation and therefore corrosion resistance. However, higher graphitisation increases the degree of hydrophobicity, which implies lower Pt adhesion to the support surface that can compromise the electrocatalyst stability.[11]

The surface chemistry of the support is therefore crucial for the anchoring of platinum nanocatalysts, and also plays a role in mass transfer and water management at high load in a PEMFC.[12] Approaches employed to modify the surface properties of carbon include grafting functional groups[13–15] and doping with heteroatoms.[16] In particular, nitrogen doping is widely used to tune electrical, chemical, and catalytic properties of carbon supports to enhance the ORR activity and durability of Pt catalysts.[17–25]

Nitrogen doping of carbon supports may improve catalyst dispersion on, and anchoring to, the surface, by enhancing porosity and charge transfer from Pt to the adjacent nitrogen atoms, which can lead to increased catalytic activity and catalyst stability.[26–30] Furthermore, the presence of nitrogen can promote the spillover effect of ORR-intermediate adsorbates (e.g. hydrogen peroxide) and their decomposition,[26,31,32] enhancing the overall electroactivity. The increased oxophilicity induced by N-doping can also promote ORR activity of the carbon itself, as demonstrated in alkaline media.[17] The introduction of pyrrolic nitrogen in the carbon structure has an impact on the corrosion resistance, leading to increased stability of Pt-based electrocatalysts.[33] Another crucial handle for increasing ORR performance at low Pt loading is the optimisation of the triple phase boundary in the catalyst layer. In this regard, the ionomer dispersion plays a significant role by facilitating efficient proton and oxygen transfer and low electrical resistance.[34] As recently demonstrated by the decrease in oxygen transport resistance (primarily attributed to O_2 transport in the ionomer film in the electrode),[15,35] the presence of nitrogen-containing groups in carbon supports increases their interaction with the sulfonic groups of the ionomer, favouring the formation of a thin conformal film of ionomer distributed over the surface of the support and leading to decreased voltage losses at high current density.[15,36] Furthermore, homogeneous dispersion of the ionomer increases accessibility to the Pt catalyst and consequently its electrochemical surface area (ECSA), and improves water management in the catalyst layer.

For all these reasons, the preparation of nitrogen-doped carbons for PEMFC cathodes has been widely investigated, and several routes have been used with this purpose, based on direct synthesis or post-treatments, including pyrolysis, chemical vapour deposition and (hydro)thermal treatments in the presence of nitrogen-containing molecules.[23,26,28–30,37–39] Compared with these procedures requiring high energy/temperature and eventually the use of metal catalysts, plasma technology is a simple and effective approach to introduce nitrogen or other heteroatoms into carbon materials, either during their synthesis (solution plasma processing)[40–42] or as a post-treatment.[41–44] The latter allows the easy surface functionalisation of pre-synthesised e.g. commercial carbon materials without affecting their bulk properties and with control over the N content by modifying the operating conditions (exposure time, gas composition, plasma power).[45] Furthermore, plasma activation is an environmentally benign process that does not use solvents or produce chemical wastes.[41] The excited state of a plasma allows modification of the surface of materials by doping as well as by etching them, further tuning the properties of the treated materials. Nitrogen functionalisation of carbon for fuel cell cathode applications has been performed

*Electrochemical Society Member.
**Electrochemical Society Fellow.
[z]E-mail: pierre-yves.blanchard@umontpellier.fr; sara.cavaliere@umontpellier.fr

using a range of gases: ammonia, nitrogen, allylamine, oxygen/nitrogen mixtures.[43,45–47] The reagents and the conditions used create different functional groups (pyrrolic-N, pyridinic-N, graphitic nitrogen, amine or ammonium groups), which drive the properties of the carbon support. Kim et al. described an increase of the Pt loading due to an increase of nitrogenated anchoring sites on the support with increase of electrochemical activity for carbon blacks doped with N_2-plasma treatment.[48] Zhang et al. demonstrated that pyridinic nitrogen functionalities were introduced in carbon nanofibres with NH_3 plasma, while pyrrolic nitrogen was formed upon N_2 plasma treatment. In both types of modified support the Pt electrochemical activity and stability were higher than those of the pristine support.[46]

In this work, Vulcan XC72 was functionalised using a nitrogen-plasma to produce doped carbons, the nitrogen content of which is related to the experimental conditions of the plasma treatment. The N-doped Vulcan carbons were characterised for their morphological, textural and structural properties, and X-ray photoelectron spectroscopy was used to determine the nitrogen speciation. Isothermal titration calorimetry was used for the first time to evaluate how the strength of ionomer-support interaction varies with the extent of functionalisation. Pt nanoparticles synthesised by a microwave-assisted polyol method in continuous flow mode from the same batch were deposited on the carbons of different nitrogen content, and the Pt/C electrocatalysts were characterised for their ORR activity and their stability on voltage cycling.

Experimental

N-doping of Vulcan XC72R carbon black.—400 mg carbon batches of the carbon black Vulcan XC72R (VC) purchased from Cabot were spread homogeneously on a Petri dish to be treated by a nitrogen plasma with a plasma generator from Europlasma including a 13.56 MHz RF generator (Integro 133 Advanced Energy) and a primary pump (Edwards). The carbon batches were pre-treated at 90 °C overnight in a vacuum desiccator (Vacuo Temp) at 280 mbar. Mass flow controllers metered a 100 sccm flow of nitrogen gas (Air Liquide 99.9999%) in the chamber. The applied power was modulated up to 300 W for a duration between 1 h and 8 h of plasma treatment. The resulting materials were labelled according to their nitrogen content (determined using elemental analysis, *vide infra*) with VC-0 being pristine Vulcan, considered as the reference, and VC-x being N-doped Vulcan contained x wt% nitrogen.

Preparation of Pt/C electrocatalysts.—Pt nanoparticles were prepared by a microwave-assisted polyol synthesis process involving a continuous flow system.[49] This system is based on a spiral borosilicate Pyrex® pipe (microwave reactor) placed perpendicularly to the microwave flow, through which a N_2-saturated precursor solution is circulated from the bottom to the top by means of a peristaltic pump. The precursor solution is prepared by dissolving 844 mg of H_2PtCl_6 $6H_2O$ (Sigma Aldrich, 99.9 wt%) in 679 ml of ethylene glycol (EG, Sigma Aldrich, $\geqslant$ 99 wt%) and adding 1.0 M solution of NaOH (Sigma Aldrich, 98 wt%) to reach a pH value of 11. The resulting solution was heated at 160 °C and flowed at 12.5 ml min^{-1} under microwave irradiation (MiniFlow 220SS Sairem) at a power of 200 W. A colloidal suspension of Pt nanoparticles (NPs) formed, which was collected and cooled in a receiver flask to stop any further reaction. The suspension of platinum nanoparticles was separated into 3 batches of 200 ml each and used for deposition on Vulcan samples with different degrees of nitrogen doping: VC-0, VC-1 and VC-3. Each batch was acidified to pH 4 by the addition of 1.0 M solution of sulfuric acid (H_2SO_4, Carlo Erba, 96 wt%) in EG, and 60 mg of carbon black were added to achieve a maximum of 60 wt% of Pt in the final Pt/C catalyst. The mixture was ultrasonicated for 30 min and stirred for 2 d to allow the Pt NPs to adsorb on the carbon support. Pt/VC materials were filtered and washed using water, water/ethanol and water, and dried at 75 °C in a vacuum desiccator. To remove any trace of EG, the samples were heated under N_2 flow at 160 °C for 1 h. The resulting catalysts were labelled Pt/VC-x (x = wt%N).

Physicochemical characterisation.— *Elemental analysis.*—The composition of the pristine and modified carbon blacks was determined by elemental analysis through combustion and pyrolysis processes. C, H, N, O, S elemental analysis was performed with a Vario Micro Cube Element Analyser.

Raman spectroscopy.—The degree of graphitisation of the samples was investigated by Raman spectroscopy using a Horiba Jobin Yvon spectrometer equipped with a blue laser diode (λ = 473 nm) and a scan surface of 100 μm^2. Raman spectra were fitted using two Lorentzian peaks centred around 1360 cm^{-1} and 1600 cm^{-1} for the D and G bands respectively and a Gaussian peak centred around 1550 cm^{-1} for the amorphous carbon.[50,51]

X-ray photoelectron spectroscopy (XPS).—The chemical speciation of the nitrogen functionalities introduced by nitrogen plasma treatment was determined by X-ray photoelectron spectroscopy (XPS) using an ESCALAB 250 spectroscope from Thermo Electron with an Al K_α ray (1486.6 eV) as monochromatic excitation source. The analysed surface area was 400 μm^2. The emitted photoelectrons were detected perpendicularly to the sample surface with a constant analyser energy mode (20 eV pass energy). Data analysis was carried out using the Avantage software. Binding energies (BEs) of all core levels are referenced to the C−C bond of C 1 s component at 284.4 eV.

X-ray fluorescence (XRF).—The platinum loading on the Pt/VC samples was determined by XRF. Samples were prepared by grinding 30 mg of Pt/VC with 160 mg of H_3BO_3. The powder was placed in a cavity and subsequently pressed to obtain a pellet of 13 mm diameter with scanned surface of *ca*. 12 mm. The same protocol was used to prepare eight standards using 0, 10, 20, 30, 40, 50, 60 wt% of Pt black (Alfa Aesar) to obtain a calibration line. The XRF analyses were performed with a PANalytical Axios Max spectrometer fitted with a Rh (4 kW) tube, and equipped with a LiF200 crystal and Omnian software.

Transmission electron microscopy (TEM).—The morphology of the carbon blacks before and after nitrogen plasma treatment were analysed by TEM using a JEOL 2200FS (Source: FEG) microscope operating at 200 kV equipped with a CCD camera Gatan USC (16 MP). Pt nanoparticles and Pt/VC electrocatalysts were analysed with a JEOL-2200FS microscope operated at 200 kV (Schottky-FEG emitter) and fitted with an in-column omega-filter, and a GATAN Ultrascan CCD 2048 × 2048 px^2 camera was used to obtain high resolution images. High-angle annular dark field STEM (HAADF—STEM) micrographs were obtained with a probe size ranging from 0.2 nm to 1 nm (convergence semi-angle of 8 mrad and collection semi-angle greater than 80 mrad). For TEM analyses, samples were suspended in ethanol and sonicated before deposition onto carbon-coated copper grids.

Nitrogen physisorption.—Nitrogen adsorption/desorption isotherms were recorded at −196 °C by means of a Micromeritics 3Flex apparatus after outgassing samples overnight at 200 °C under vacuum (10^{-5} Torr). The specific surface area (S_{BET}) was calculated using the Brunauer–Emmett–Teller (BET) equation[52] and taking 0.162 nm^2 as the cross-sectional area of one N_2 molecule. The pore size distributions (PSD) were calculated by using the SAEIUS software for the 2D non-local density functional theory (2D-NLDFT).[53]

X-ray diffraction (XRD).—Powder XRD patterns of Pt/VC-x materials were recorded at 20 °C in Bragg-Brentano configuration using a PANalyticalX'pert diffractometer, equipped with a hybrid

monochromator, operating with CuK_α radiation ($\lambda = 1.541$ Å), and using a step size of 0.1° 2θ within the 2θ domain from 20 to 70°. The XRD samples were prepared by depositing the powder onto the XRD holder, which was sealed using Kapton tape.

Ionomer/support interaction by isothermal titration calorimetry.— For the isothermal titration calorimetry (ITC), a TAM III thermostat (TA Instruments) equipped with 3 nanocalorimeters with a detection limit of 10 μJ was used to perform heat flow measurements at 25 °C. Titration and reference vials made of stainless steel with a volume of 1 ml were used. For the measurements, 800 μl of pristine and nitrogen doped Vulcan XC72R suspensions in a mixture of deionised water and 1-propanol (16/84) at 1–10 mg ml^{-1} were prepared. 25 aliquots of 10 μl for each ionomer dispersion in the same solvent mixture at 0.2–2 wt% were injected. Between the injections, an interval time of 45 min was set, to allow equilibrium to be reached after each titration step. The samples were stirred during the measurements to prevent sedimentation of the carbon during the 24 h' duration of the experiment. The reference vial was filled with a mixture of deionised water and 1-propanol (16/84) and the 25 aliquots were added as for the titration. Every titration was made simultaneously on the 3 nanocalorimeters to check the reproducibility of the results.

Electrochemical measurements.—Electrochemical analysis was carried out in a three-electrode cell comprising a high temperature rotating disk electrode (HT RDE, geometric area 0.196 cm^2, Pine Instruments, working electrode), a reversible hydrogen electrode (RHE, reference electrode) and a graphite rod (counter electrode) monitored with a Bio-Logic SP-300 instrument. All the potential values are referred to the RHE.

Ink formulations.—Carbon inks were prepared by dispersing 2 mg in 860 μl of isopropanol (Aldrich)/ ultrapure water Milli-Q grade (20/80) and 40 μl of 5 wt% Nafion® dispersion in lower aliphatic alcohols and water (Aldrich) by ultra-sonication for 1 h in an ice/water bath. 7 μl of the resulting colloidal suspensions were deposited onto the RDE surface with a micropipette (leading to a loading of 80 μg_{carbon} cm^{-2}), and then the electrode was dried in an oven at 70 °C for ∼15 min.

For the catalyst ink, Pt/C was added to water/1-propanol (80/20) solvent mixture to obtain a Pt loading of 20 μg cm^{-2}. A 5 wt% Nafion® solution was added to form the ink. 20 μl of ink were deposited on the glassy carbon part of the electrode mounted on the inversed rotating shaft and the rotation was set at 200 rpm to dry the ink.

ORR activity measurements.—Prior to the experiment, the cell was filled with 0.1 M $HClO_4$ electrolyte and purged with N_2 gas. 25 cycles of cyclic voltammetry at 100 mV s^{-1} at 0.05 V to 1 V vs RHE were performed to clean the catalyst surface, then three cycles were recorded at 20 mVs^{-1} to measure the Pt electrochemical surface area (ECSA). The CO stripping technique was carried out after 5 min of CO bubbling and 20 min of N_2 purging, by holding at 0.1 V vs RHE with a chronoamperometry (CA) technique. Three cycles of CV from 0.05 V to 1 V at 20 mV s^{-1} were recorded. The first cycle shows the CO stripping peaks whereas the second cycle is used as baseline.

The mass activity (MA) was determined using linear sweep voltammetry (LSV) from 0.05 V to 1.1 V vs RHE at 20 mV s^{-1} under O_2 at 1600 rpm. The baseline was realised with a N_2 saturated electrolyte (LSV from 0.05 V to 1.1 V vs RHE at 20 mV s^{-1} under N_2 at 1600 rpm).

Accelerated stress tests (AST) for carbon corrosion.—Two types of AST were used to evaluate carbon corrosion on bare and Pt catalysed carbon blacks with different degree of N-doping:

- Potentiostatic accelerated stress tests were performed on the carbons by holding the working electrode potential at 1.2 V vs RHE for 2 h in 0.5 M H_2SO_4 (95%–98% ACS reagent, Honeywell Fluka) at 80 °C whilst recording the current. In order to heat the electrolyte uniformly, a jacketed cell with a circulation thermostat was used. Prior to the experiments, the electrolyte solution was purged with nitrogen (Air Liquide, > 99.999%) for at least 30 min, whilst during electrochemical experiments a nitrogen atmosphere was kept above the solution.
- An accelerated stress test was performed by cycling an electrode bearing Pt/VC from 1.0 V to 1.5 V vs RHE during 60,000 cycles at 500 mV s^{-1} in 0.1 M $HClO_4$ N_2 saturated electrolyte at 25 °C. The Pt ECSA was recorded at 20 mV s^{-1} every 1,000 cycles.

Results and Discussion

Compositional, textural and morphological characterisation and nitrogen speciation.—Vulcan XC72R carbon blacks were modified under nitrogen plasma treatment. In order to vary the amount of nitrogen introduced in the carbon support, different exposure times (up to 8 h) and plasma power (up to 300 W) were applied and the different batches obtained were qualitatively and quantitatively characterised.

Elemental analysis (EA) was performed on the prepared samples to assess the amount of nitrogen introduced by the plasma treatment in the different conditions explored. Experiments were conducted by increasing the power from 0 to 300 W keeping the duration at 1 h, and by increasing the duration of the treatment from 0 to 8 h when keeping the maximum power (300 W). First of all, EA confirms the successful doping by nitrogen of carbon upon N_2-plasma treatment, when 5% of nitrogen doping is achieved after 8 h' treatment under 300 W plasma. Secondly, the nitrogen content was observed to increase linearly with the time of treatment and with the power of the plasma (Fig. 1).

In Table I are listed the chemical compositions evaluated by EA of Vulcan XC72 before and after N_2-plasma treatment at 300 W for durations of up to 8 h. Considering the overall sample composition, it is evident that plasma treatment also introduced oxygen into the carbon support, since for all samples there is an increase of *ca* 1% compared to pristine VC-0. This is in agreement with the etching capability of plasma, which induces structural defects and unsaturated edge carbon atoms which easily react with oxygen when exposed to air to form oxygen-containing groups.[45]

X-ray photoelectron spectroscopy (XPS) identified the different types of nitrogen functionalities introduced on the carbon black surface with the plasma treatment and confirmed the chemical doping of nitrogen on carbon. In particular, the XPS spectra of pristine carbon VC-0 and 3 wt% N-doped carbon VC-3 were compared. The deconvolution of the C 1 s spectrum of Vulcan before and after nitrogen plasma treatment is shown in Fig. 2. Four carbon contributions were determined, corresponding to C sp^2, C sp^3, C–O and C=O centred at 284.4 eV, 285.1 eV, 286.0 eV and 287.4 eV, respectively. After nitrogen plasma treatment, the C sp^2 contribution decreased to the benefit of the others, and C–N groups[54] are superimposed on the C–O peak centred at 286.3 eV.

The XPS spectrum of VC-0 presents no peak in the N 1 s region, while the sample bearing 3 wt% N presented three peaks centred at 399.0 eV, 400.2 eV and 401.5 eV (Fig. 3a). These peaks correspond to pyridinic, pyrrolic and graphitic nitrogen respectively[55] (represented schematically in Fig. 3b): pyrrolic-N (1) is bonded to two carbon atoms in a 5 atom aromatic ring and contributes to the π system with two p-electrons; "graphitic" or "substituted" nitrogen (2) is a quaternary nitrogen in which nitrogen atoms are incorporated into the graphene layer by replacing carbon atoms; pyridinic-N (3) is at the edge of graphene planes bonded to two carbon atoms and donates one p-electron to the aromatic π system. Furthermore, peaks were observed corresponding to amine groups (4) and N-oxides of pyridinic-N (bonded to two carbon atoms and one oxygen atom) (5).

XPS also allowed the quantification of surface nitrogen, which was compared to the values determined by elemental analysis and relative to the bulk material composition. As summarised in Table II, in each case the nitrogen content obtained from XPS is higher than

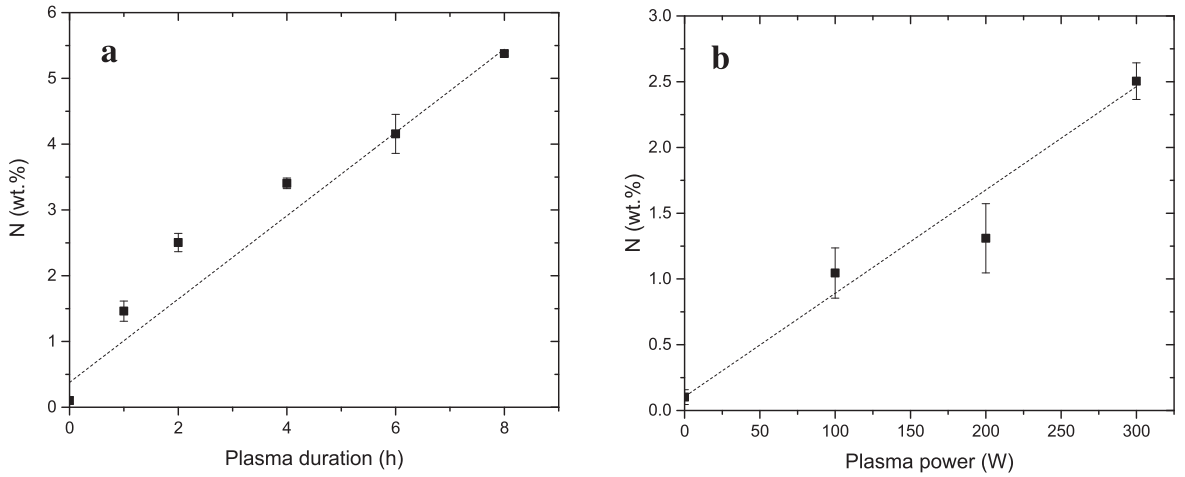

Figure 1. Relationship between nitrogen content on VC carbon black and (a) duration, using a plasma of 300 W and (b) power, for 1 h plasma treatment.

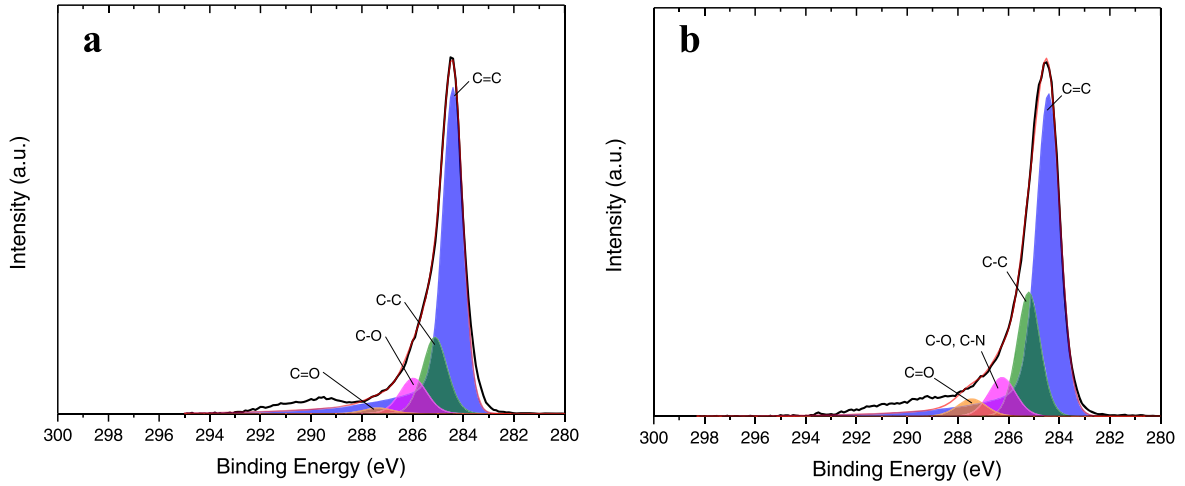

Figure 2. High-resolution C 1 s XPS spectra of Vulcan carbon black before (VC-0, (a) and after a nitrogen-plasma treatment of 3 h (VC-3, (b), and assignments of the various contributions.

that measured by EA; for the VC-3 sample, the N/C ratio obtained by EA is 0.037 while it is 0.081 by XPS. This result indicates that the nitrogen is introduced predominantly on the surface of the carbon by the plasma treatment, without significantly affecting its bulk properties. Independently from the duration of the plasma treatment and of the resulting total nitrogen amount introduced, the relative percentage of the different types of nitrogen was the same: 31%–32% pyridinic-N, 30%–31% amine, 23%–24% pyrrolic-N, 11% graphitic-N and 4%–5% N-oxides (Table II).

N_2 plasma treatment incorporates nitrogen into the carbon structure, also creating structural defects and unsaturated carbon atoms prone to oxidation. Raman spectroscopic analysis was performed on VC-0 and VC-3 to evaluate the modification to the VC structure upon plasma treatments of different durations (Fig. S1 (available online at stacks.iop.org/JES/169/044502/mmedia), Supplementary Material). Raman spectra of all samples display two bands at 1580 cm^{-1} (G band) and 1350 cm^{-1} (D band), both resulting from the vibrations of sp^2 carbon atoms. The D band corresponds to the breathing mode of the sp^2 carbons in aromatic rings, which is related to defects, whereas the G band corresponds to the in-plane bond-stretching motions of the sp^2 carbons in aromatic rings, informing on the graphitic properties of the material. For each

Table I. Chemical compositions of Vulcan XC72 before and after N_2-plasma treatment at 300 W for various durations (VC-x) and after N_2-plasma treatment for 2 h at various powers (VC-Py with y the plasma power in W), evaluated by elemental analysis.

Sample	Plasma treatment duration (h)	Plasma treatment power (W)	C (wt%)	N (wt%)	S (wt%)	O (wt%)
VC-0	—	—	96.57 ± 2.34	0.10 ± 0.06	0.88 ± 0.20	2.48 ± 1.90
VC-1	1	300	94.65 ± 0.04	1.46 ± 0.15	1.02 ± 0.16	3.31 ± 0.40
VC-2	2	300	92.05 ± 1.87	2.50 ± 0.14	1.09 ± 0.19	4.63 ± 1.66
VC-3	4	300	92.95 ± 1.15	3.40 ± 0.08	0.40 ± 0.47	3.02 ± 1.15
VC-4	6	300	92.18 ± 0.62	4.16 ± 0.30	0.44 ± 0.52	3.34 ± 1.70
VC-5	8	300	92.52 ± 0.03	5.38 ± 0.04	0.75 ± 0.13	3.38 ± 0.23
VC-P100	2	100	95.65 ± 0.67	1.05 ± 0.19	0.92 ± 0.08	2.68 ± 0.47
VC-P200	2	200	95.60 ± 0.94	1.31 ± 0.26	1.09 ± 0.18	3.09 ± 1.60

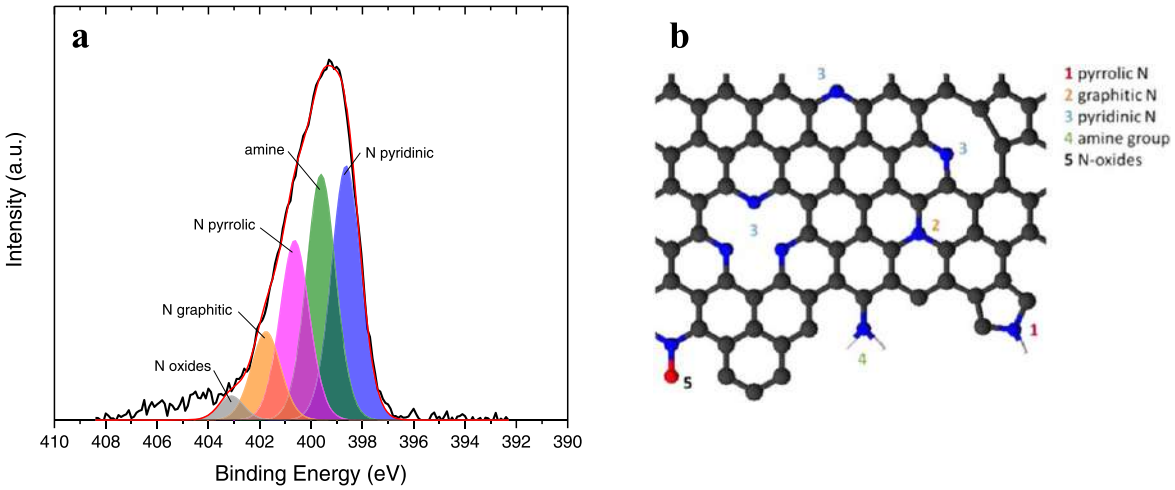

Figure 3. High-resolution XPS spectrum of the N 1 s region of VC-3 (a) and structure of the nitrogen configurations introduced in the carbon structure by nitrogen plasma treatment (b).

sample, the degree of graphitisation, corresponding to the ratio of integrated peak areas of the D band and the G band ($I_D/I_{G,}$) was calculated, as well as the in-plane graphitic domain size L_a (Table III), according to Eq. 1.[56] The ratio of the integrated intensity gives information on the degree of disorder in the carbon structure, which is inversely proportional to the graphitic domain size.

$$L_a = (2.4 \times 10^{-10})\lambda_l^4 \left(\frac{I_D}{I_G}\right)^{-1} \quad [1]$$

The results of Table III indicate that the N_2-plasma treatment led to a minor decrease of the size of the graphitic domains, less than 1 nm in all samples. After 4 h plasma treatment an increase of the I_D/I_G ratio is observed, which indicates an increase of disorder in the carbon structure, in agreement with the introduction of nitrogen and the creation of defects in the VC surface and not in the bulk.

The effect of the duration of the plasma treatment on the carbon black morphology was evaluated by transmission electron microscopy (TEM). The TEM micrographs of samples before and after the functionalisation at different exposure times are presented in Fig. 4.

The pristine carbon black,VC-0, comprised carbon particles of diameter *ca* 50 nm embedded in a continuous matrix (VC-0 Fig. 4a).[33] This matrix is gradually removed upon nitrogen plasma treatment of 1 h (VC-1 Fig. 4b) and 4 h (VC-3 Fig. 4c), revealing well-dispersed spherical particles of *ca* 25 nm. This result suggests that the continuous matrix may be amorphous carbon, which is removed by the highly reactive plasma treatment with etching capability.[57] It can be noticed that Raman spectroscopy did not evidence increased graphitisation, supporting this interpretation. This is likely due to the combined effect of amorphous matrix removal and increased disorder due to the structural defects in carbon upon introduction of nitrogen atoms, giving rise to an overall slight modification of the I_D/I_G ratio. Furthermore, Raman spectroscopy is a surface measurement from in-plane optical phonons, therefore more sensitive to the functionalisation performed by plasma treatment.[58]

Nitrogen adsorption-desorption measurements and pore size distribution (PSD) calculations were performed to monitor eventual evolution of the surface area and porosity characteristics of the carbon upon N_2-plasma treatment.[59] Unmodified carbon VC-0 possesses specific surface area (S_{BET}) of 230 $m^2\ g^{-1}$ and contains mesopores and micropores.[15] Analysis of the micropore surface area by SAEIUS (2D-NLDFT)[53] leads to the determination of the mesopore+macropore (external) surface area by simple difference with the BET surface area. It was observed that the S_{BET} was lower by 7% compared to pristine carbon black after 1 h of N_2-plasma treatment, and reduced by 30% after 4 h (Table IV). Despite the decrease in the total S_{BET}, the proportion of the surface area in mesopores is essentially unchanged upon the N_2 plasma treatment (see Table IV).

Quantification of support/ionomer interaction.—The expected benefit of a strong support/ionomer interaction is the formation of a thin, conformal film of ionomer distributed over the surface of the support that will be less susceptible to displacement from the carbon surface at high current density.[15,35] The Nafion® fuel cell ionomer is a perfluorosulfonic acid (PFSA) consisting of a hydrophobic poly (tetrafluoroethylene) (PTFE) backbone and perfluorinated ether side chains with terminal sulfonic acid groups (SO_3H). The interaction of Nafion® with the carbon support strongly depends on the surface properties of the latter as well as its structure, porosity and degree of graphitisation. Due to the hydrophilicity of the carbon surface, Nafion® is probably adsorbed via the polar sulfonic groups on VC, while it is rather interacting via the PTFE main chain with more hydrophobic carbonaceous materials.[60] Isothermal titration calorimetry (ITC) was used to investigate the strength of the interaction between Nafion® and Vulcan XC72 and any evolution with N-doping. This technique was recently demonstrated to be a useful tool for the investigation of the adsorption of PFSA on carbon black with the determination of thermodynamic parameters.[59]

In this work, three suspensions of VC with different nitrogen contents (0, 2, 3 wt%, labelled VC-0, VC-2 and VC-3, respectively) in water/1-propanol were titrated with a dilute dispersion of Nafion® EW1100. The thermograms corresponding to the heat flow recorded during the injection of Nafion® into the three VC suspensions are shown in Fig. 5. The result of the blank (reference) experiment is also shown, consisting of the "titration" (dilution) of Nafion® in the water/1-propanol solvent without carbon present. This enables a correction to be made for the influence of the enthalpy of mixing on the overall heat flow. In all cases, the results of Fig. 5 indicate that the timescale of 45 min was enough for the decay of the heat flow to the baseline level, meaning that despite the size of the Nafion®, the kinetics is relatively fast.

The experimental conditions used and the method were validated by these results: the injection of the ionomer dispersion into the carbon suspensions resulted in exothermic peaks whereas dilution peaks are endothermic (reference, green line). The sorption contribution is high and intense compared to the dilution signal, meaning that the interaction between carbon and ionomer is clearly demonstrated. Furthermore, the carbon blacks doped with nitrogen gave rise to different thermograms with different heat flow intensities and inflections. To compare the three experiments, the cumulative heat release due to ionomer adsorption measured by ITC is depicted in Fig. 6.

Table II. Comparison between nitrogen content values obtained by elemental analysis and from XPS for samples VC-1 and VC-3.

Sample	EA		XPS						
	N (wt%)	N/C	Pyridinic-N (wt%)	Amine (wt%)	Pyrrolic-N (wt%)	Graphitic-N (wt%)	N-oxides (wt%)	N total (wt%)	N/C
VC-1	1.46 ± 0.15	0.015	0.96	0.94	0.75	0.35	0.14	3.14	0.034
VC-3	3.40 ± 0.08	0.037	2.28	2.21	1.62	0.8	0.19	7.1	0.081

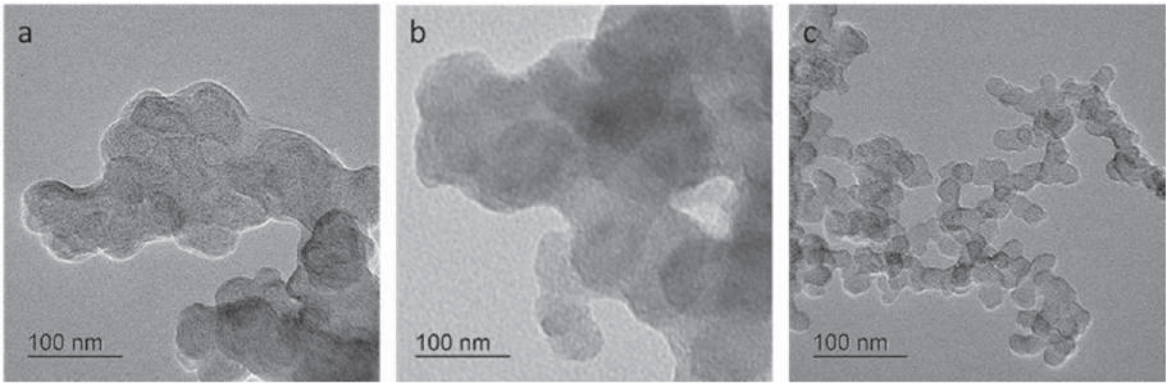

Figure 4. TEM micrographs of Vulcan: VC-0 (a), VC-1 (b) and VC-3 (c).

Table III. Ratio I_D/I_G and in-plane graphitic domain size L_a determined from Raman spectra of VC samples before and after N_2-plasma treatment.

Sample	I_D/I_G	L_a (nm)
VC-0	4.1	2.9
VC-3	4.4	2.7

It can be observed in Fig. 6 that for each sample the heat release progressively increases with the ionomer injections up to a certain value, after which a plateau is reached. This amount of adsorbent needed to reach the onset of the plateau increases as the nitrogen content in the carbon black increases, such that the plateau is achieved after about additions 0.14 mg of Nafion® (equivalent to 0.016 mM SO_3H/g carbon) for VC-0, 0.35 mg of Nafion® (equivalent to 0.040 mM SO_3H/g carbon) for VC-2 and about 0.84 mg of Nafion® (equivalent to 0.095 mM SO_3H/g carbon) for VC-3.

These amounts are not proportional with the BET specific surface area, meaning that the heat effect is influenced by the accessibility but probably correlated to the surface chemical composition. Once the plateau is reached, additional injections have no influence, indicating that equilibrium is reached. Initially, the most energetic sites (defects, kinks, surface roughness) are covered by the ionomer, leading to the strongest heat release during adsorption. Later, a lower increase of heat release is observed when injecting ionomer since the adsorption takes place at lower-energy sites. The plateau might be ascribed to the successive adsorption of Nafion® onto Nafion® that is already adsorbed on the carbon and is not detected by ITC, but was reported in a study based on ^{19}F NMR characterisation.[60]

The heat release, and thus the strength of the carbon/ Nafion® interaction, is also very different on the three carbon samples and strongly depends on the degree of nitrogen functionalisation of the XC72R. The strongest heat release for each aliquot of ionomer is observed for the Vulcan functionalised with the highest amount of nitrogen (3 wt%, VC-3), and the lowest for the pristine Vulcan XC72R. Thus, the following trend of Nafion®/carbon support interaction strength is seen: VC-3 > VC-2 > VC-0.

The normalised representation of Fig. 6 allowed the calculation of the adsorption enthalpy $-\Delta H$ (in kJ per mol of SO_3H) and thereby the quantification of the strength of the interaction between the ionomer and the carbon support. This is achieved by the determination of the slope before the plateau where an equilibrium is reached (Table V).

Except the work of Thoma,[59] based on a slightly different approach to estimate the enthalpic contribution, very few studies have focused on similar system. Direct determination of the adsorption enthalpy of sodium dodecyl sulphate onto carbon blacks obtained by González-García et al.[61] revealed twice higher ΔH in the low concentration range. Nevertheless, since the enthalpic effects are impacted by both the sorption within and outside the porosity, and by the organization at the interface,[62] it is undoubtedly difficult to discriminate these various contributions for the Nafion®/carbon blacks interface. Very low adsorption enthalpy is obtained for VC-0 and it increases with increase in the nitrogen content of the carbon blacks. This is in line with the conclusions by González-García et al.[61] where contribution from the surface chemical composition was noticed despite the differences of textural properties. This demonstrates the role of the heteroatom in promoting the adsorption of the ionomer on the carbon surface, inferring that the interaction occurs between the SO_3H groups of Nafion® and the nitrogen of the doped support. In conclusion, ITC experiments demonstrated that increasing the amount of nitrogen on the carbon black strengthens the interaction with the ionomer, with potential impact on catalyst and fuel cell performance and durability.

Electrochemical characterisation.—To evaluate the effect of nitrogen functionalisation on the electrochemical corrosion resistance, the corrosion charge of the N-doped and undoped Vulcan carbon was measured by chronoamperometry at high potential and high temperature in acid medium. In particular VC-0, VC-1 and VC-3 were characterised, allowing an eventual trend with increasing nitrogen content from *ca* 1 to 3 wt% to be evaluated. The corrosion of the carbon supports was quantified by electrochemical oxidation at 1.2 V vs RHE for 2 h at 80 °C. This potential value was selected in order to discriminate among the investigated carbons (at continuous hold at 1.4 V vs RHE, all carbon blacks were rapidly corroded). The electrochemical degradation was estimated from the integrated

Table IV. Specific surface area (S_{BET}) and surface ($S_{\mu pores}$) of micropores for pristine and N-doped carbon blacks.

Sample	S_{BET} ($m^2\ g^{-1}$)	$S_{NL\text{-}DFT}$ ($m^2\ g^{-1}$)	$S_{\mu pores}$ ($m^2\ g^{-1}$)	$S_{mesopores}$ ($m^2\ g^{-1}$)
VC-0	230	239	188	51
VC-1	213	220	173	47
VC-3	160	160	110	50
VC-4	154	144	101	43
VC-5	141	132	90	42

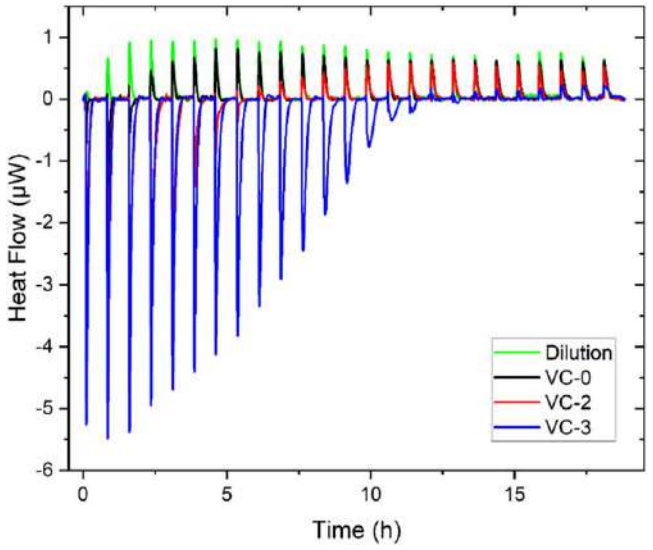

Figure 5. Heat flow during titration of Nafion® with non-modified (VC-0) and nitrogen-doped (VC-2, VC-3) carbon black Vulcan XC72R suspended in water/1-propanol or with the solvent mixture as a reference (dilution).

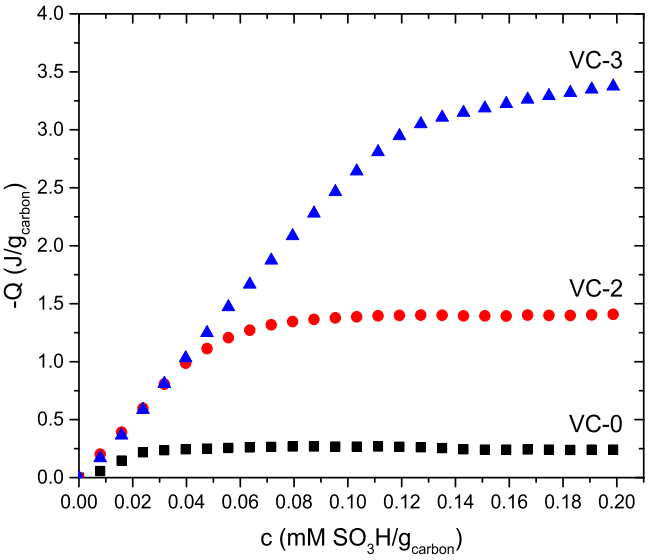

Figure 6. Cumulative heat release during titration of Nafion® with non-modified and nitrogen-doped carbon black Vulcan XC72R suspended in water/1-propanol normalised by carbon mass: VC-0 (black squares), VC-2 (red dots) and VC-3 (blue triangles).

corrosion current (corrosion charge normalised by the carbon mass) and compared to the value obtained for VC-0. For the carbons with increased nitrogen content there is a slight decrease in the corrosion charge with the lowest charge observed for the sample bearing the highest amount of nitrogen, VC-3 (Table VI). The corrosion charge of this sample is 20% lower than that of the parent VC-0.

It is reasonable to take into account the different specific surface areas, which may affect the surface reactivity to corrosion and oxidation. Therefore, the specific corrosion charge relative to the surface area (rather than the sample mass) was calculated. The normalised corrosion charge slightly increases with increasing nitrogen content in the carbon. In an attempt to confirm the trend observed in these results, an accelerated stress test promoting carbon degradation was applied to catalysed carbon blacks. The next paragraphs describe the physico-chemical and electrochemical characterisation of Pt deposited on undoped (VC-0) and 3 wt% N-doped carbon (VC-3).

Structural characterisation.—Platinum nanoparticles were prepared by microwave-assisted polyol method in a flow system.[49] This allowed the subsequent deposition of the same batch of NPs on to undoped (VC-0) and N-doped (VC-3) carbon blacks, to evaluate and discriminate between the properties of the support and its interaction with the nanocatalyst.

XRF results indicated a Pt loading of *ca* 50 wt% for the Pt/VC-0 and Pt/VC-3 electrocatalysts (Table VII).

To remove ethylene glycol eventually blocking the NP surface and that can negatively affect their electrocatalytic activity, mild thermal treatment was performed on the Pt/VC-x materials. The NPs size observed on the two catalysed supports was similar: the NPs on Pt/VC-3 are slightly bigger (2.7 nm) than those on Pt/VC-0 (2.6 nm)[63] (Figs. 7a and 7b, S2a and S2b in Supplementary Material). Furthermore, the dispersion of the platinum nanoparticles is more homogeneous on the N-doped carbon than on the pristine support. These results provide evidence for the role of the carbon surface in anchoring the Pt nanocatalysts, wherein the N-doped carbon black interacts more strongly with Pt (see XPS results) and promotes their more homogeneous dispersion upon thermal treatment.

Their XRD diffractograms (Fig. 8) display diffraction peaks at $2\theta = 39.7°$, 46.2° and 67.4°, characteristic of platinum (JCPDS 004 0802). The Scherrer equation was applied to the Pt (111) peak, allowing estimation of the average size of the Pt crystallites as around 4 nm, whereas the particle size assessed by TEM was 2.6–2.7 nm.

The surface chemistry of the Pt/VC-x electrocatalysts was analysed by XPS (Fig. 9). The Pt 4 f spectra were deconvoluted using three doublets with an energy gap of 3.35 eV corresponding to 7/2 and 5/2 spin–orbit splitting of Pt^0, Pt^{2+} and Pt^{4+}.

The 7/2 contributions are centred at the binding energies 71.24 eV, 72.25 eV and 73.25 eV respectively and the 5/2 contribution at the binding energies 74.56 eV, 75.6 eV and 76.62 eV.[64]

The higher amount of oxidised platinum in Pt/VC-3 compared to Pt/VC-0 (29% vs 26%, see Table SI in Supplementary Material) may be attributed to an increased strength of interaction with the support, characterised by enhanced electron transfer from Pt to carbon due to the presence of N atoms incorporated on the surface.[65] Furthermore, there is a slight energy shift to higher binding energy (+0.13 eV) between the reference and the nitrogen-doped Pt/VC-3 sample (Fig. 9), which also suggests the presence of a low-coordinated electronic state of Pt with electron transfer towards the support leading to relative positive charge on Pt.[30,65] The spectra of the N 1 s region of the catalysed supports (Fig. S3) display peaks characteristics of the three types of nitrogen speciation (graphitic, pyrrolic and pyridinic) already discussed for the non-catalysed support in Fig. 3 and Table II. However, these peaks are significantly downshifted to lower binding energy for the catalyst supported on N-doped carbon

Table V. Adsorption enthalpy obtained by determination of the slope on ITC experimental data with Nafion® and undoped and N-doped carbon blacks.

Sample	N content (wt%)	$-\Delta H$ (kJ mol SO_3H^{-1}) adsorption enthalpy
VC-0	0.10 ± 0.06	6.7 ± 0.5
VC-2	2.5 ± 0.14	24.3 ± 0.2
VC-3	3.10 ± 0.07	26.0 ± 0.1

Table VI. Corrosion charge and area specific corrosion charge for pristine and N-doped Vulcan carbon.

Sample	Corrosion charge (C mg^{-1})	Area specific corrosion charge (C m^{-2})
VC-0	1.94	8.42
VC-1	1.71	8.03
VC-3	1.55	9.69

Table VII. Platinum loading (XRF) of the catalysts Pt/VC-0 and Pt/VC-3, and their electrochemically active surface area (ECSA), mass (MA) and specific activities (SA) at 0.9 V vs RHE at beginning of test. In parenthesis are indicated the values obtained at end of test, *i.e.* after the AST from 1.0 V to 1.5 V vs RHE during 60,000 cycles at 500 mV s^{-1} in 0.1 M $HClO_4$ N_2 saturated electrolyte at 25 °C.

Sample	XRF		$ECSA_{Hupd}$ (m^2 g_{Pt}^{-1})	$ECSA_{CO}$ (m^2 g_{Pt}^{-1})	$MA_{0.9\ V}$ (A mg_{Pt}^{-1})	$SA_{0.9\ V}$ (mA cm^{-2})
	Pt (wt%)	C (wt%)				
Pt/VC-0	49.6	48.9	48 (30)	45 (27)	0.251 (0.123)	0.528 (0.407)
Pt/VC-3	51.1	47.8	51 (28)	51 (31)	0.293 (0.179)	0.576 (0.645)

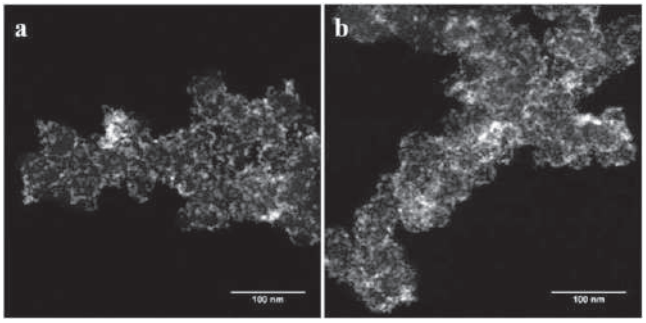

Figure 7. HAADF-STEM micrographs of Pt/VC-0 (a) and Pt/VC-3 (b).

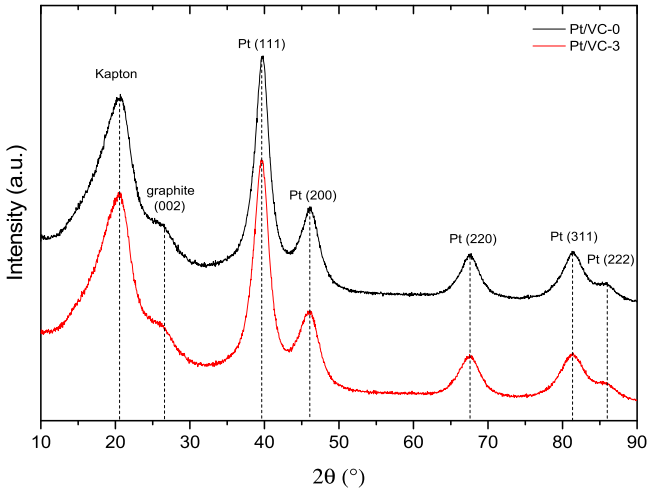

Figure 8. XRD diffractograms of Pt-VC-0 and Pt/VC-3.

compared to the bare support (−0.35 eV for the N-pyridinic, −0.41 eV for the N-pyrrolic and −0.49 eV for the N-graphitic). Again, this can be related to the interaction with Pt, and the effect is complementary to that observed for the Pt 4 f signals, i.e. there is greater electron density on the nitrogen groups upon interaction with the electron donor Pt. These observations are consistent with the existence of a strong metal-support interaction between the Pt and N-doped carbons,[30,65] which can have a crucial role in anchoring and stabilising the metal catalyst on the support surface.

Electrochemical characterisation of the undoped Pt/VC-0 and N-doped Pt/VC-3 electrocatalysts led to evaluation of their electrochemical surface area (ECSA) and their activity towards ORR, as well as their retention upon accelerated stress testing (AST). The ECSA was determined from the H_{upd} desorption and from the CO stripping results (Table VII). Cyclic voltammetry (CV) measurements on the Pt/VC-0 and N-doped Pt/VC-3 electrocatalysts in acidic medium under nitrogen show the characteristic hydrogen adsorption/desorption peaks in the 0.05–0.4 V vs RHE potential range and the Pt oxide formation/reduction at potential > 0.8 V and 0.5–1.0 V vs RHE, respectively (Fig. S4a in Supplementary Material). Pt ECSA was calculated from the hydrogen desorption peak and had the same value of around 50 $m^2g_{Pt}^{-1}$ for both catalysts. While Pt ECSA are similar, TEM images show different particle dispersions and should induce smaller ECSA when nanoparticles are agglomerated. The ECSA obtained using the CO stripping is similar to that obtained by H_{upd}.

CV measurements on the catalyst in acidic medium after CO adsorption show two peaks of CO desorption at 0.75 V and 0.85 V vs RHE (Fig. 10). Different explanations have been proposed to rationalise the existence of these two peaks, including desorption from different Pt surface crystallographic planes, or from particles of different size and degree of agglomeration, the presence of surface defects, and the Pt loading.[66] As the Pt particles in this work resulted from the same batch of polyol synthesis for both Pt/VC-0 and Pt/VC-3, they should have the same size distribution and the same exposed surface planes.[67] However, HAADF-STEM analysis revealed slightly different average NP size for Pt/VC-0 and Pt/VC-3, which should not have a significant impact on CO stripping peaks. The stripping peak at lower potential is considered to be related to Pt nanoparticle agglomerates whereas the higher potential peak is related to isolated Pt nanoparticles.[68] The high Pt loading (50 wt %) can lead to two CO stripping peaks by favouring the Pt nanoparticle agglomerates.[69] The pristine catalyst shows a high potential peak of twice the intensity of the low potential peak, indicating that the majority of nanoparticles are isolated. In contrast, for the N-doped catalyst the two CO stripping peaks have same intensity, indicating the presence of isolated nanoparticles and agglomerates in similar proportions. Upon AST, a decrease in the intensity of CO stripping peaks is observed for both catalysts. For the catalyst on the undoped support, the ratio of peak intensities is reversed as carbon corrosion leads to the agglomeration of isolated nanoparticles, whereas the catalyst with the N-doped retained its proportions of isolated nanoparticles and agglomerates, indicating a better stability.

ORR activity was evaluated by LSV on Pt deposited on undoped and N-doped supports at beginning of test (BoT) and at end of test (EoT), i.e. after 60,000 cycles of an AST at high potential (Figs. 11 and S4b in Supplementary Material). The voltammogram shapes are characteristic of oxygen reduction reaction reaching a diffusion

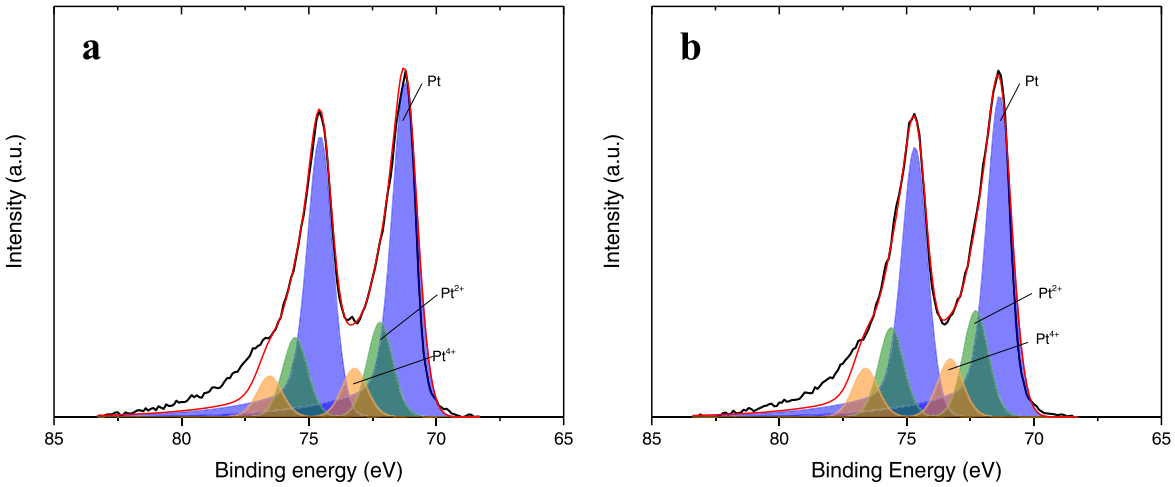

Figure 9. High-resolution XPS spectra of the Pt 4 f region for Pt/VC-0 (a) and Pt/VC-3 (b).

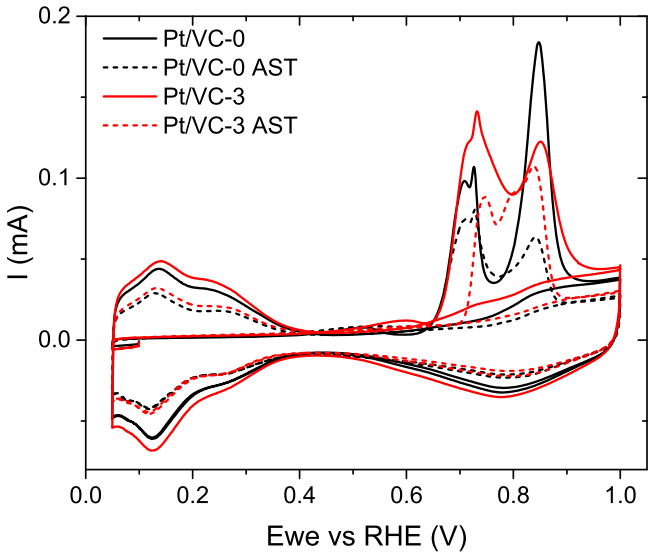

Figure 10. Cyclic voltammograms in CO free 0.1 M $HClO_4$ at a sweep rate of 20 mV s^{-1} after CO adsorption for Pt/VC-0 and Pt/VC-3 before (solid line) and after AST (dashed line).

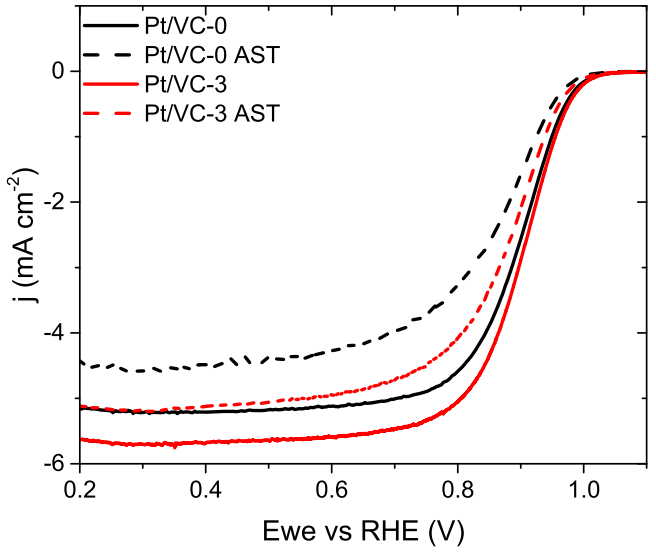

Figure 11. Voltammograms in O_2 saturated 1 M $HClO_4$ at a sweep rate of 20 mV s^{-1} at 1600 rpm for Pt/VC-0 and Pt/VC-3 before (full line) and after AST (dashed line).

limited current density plateau close to the theoretical value at 1600 rpm (5.7 mA cm^{-2}). The BoT voltammograms in oxygen saturated electrolyte show a similar onset potential at 0.97 V vs RHE for both catalysts. The mass activity (MA) at 0.9 V vs RHE was higher for the catalyst based on N-doped carbon than for Pt/VC-0 (0.293 vs 0.251 A mg_{Pt}^{-1}) (Fig. 11). At EoT, the mass activity decreased for both catalysts but to a lesser extent for Pt supported on N-doped Vulcan: the MA of the Pt/VC-0 decreased by 51% (from 0.251 to 0.123 A mg_{Pt}^{-1}), while that of Pt/VC-3 of 39% (from 0.293 to 0.179 A mg_{Pt}^{-1}) (Table VII). Due to a slightly higher decrease in UPD determined ECSA in the latter catalyst, its surface activity (SA), very similar at beginning of test (BoT), became significantly higher at end of test (EoT) compared to that of Pt/undoped Vulcan (0.645 vs 0.407 A cm^{-2}).

To conclude, Pt/VC-3 showed better beginning of test (BoT) and end of test (EoT) activity than Pt/VC-0, with a similar ECSA loss upon AST. This increased ORR performance and stability at high voltage can be attributed to the support surface. On the one hand, N-doped carbon gives stronger anchoring sites for Pt than undoped carbon black and the possibility of promoting ORR due to its oxophilicity.[17] On the other hand, Vulcan treated under N_2-plasma presents higher corrosion resistance, which can be attributed to the presence of pyrrolic nitrogen.[33]

Conclusions

Nitrogen-plasma treatment of Vulcan carbon leads to carbon surface functionalisation with the control of the introduced nitrogen content and preservation of the porosity characteristics. Using calorimetry and surface analysis methods, the introduction of nitrogen functionalities was demonstrated to strengthen the interaction of the N-doped carbon with both Nafion® ionomer and with Pt nanoparticles. The effect of such interactions was demonstrated with improved catalyst dispersion, and enhanced ORR activity and durability in electrochemical accelerated stress tests. This approach can be further extended to carbons synthesised with tuned morphology and porosity, which is expected to further improve their properties in the fuel cell catalyst layer, with significant impact on PEMFC performance and durability.

Acknowledgments

The research leading to these results has received funding from the GAIA project, which receives funding from the Fuel Cells and

Hydrogen 2 Joint Undertaking (now Clean Hydrogen Partnership) under grant agreement No 826097 and IMMORTAL project, which receives funding from the Fuel Cells and Hydrogen 2 Joint Undertaking (now Clean Hydrogen Partnership) under grant agreement No 101006641. This Joint Undertaking receives support from the European Union's Horizon 2020 research and innovation programme, Hydrogen Europe and Hydrogen Europe Research. SC acknowledges IUF for financial support. The authors acknowledge discussions with Prof. Jerzy Zajac and Mr Amine Geneste from ICGM on calorimetry measurements and Dr Frédéric Pailloux from Institut P' on STEM analysis. The authors thank Julien Fullenwarth for technical assistance for the XRF and XRD measurements, and Valérie Flaud for support with the XPS measurements.

ORCID

Alice Parnière https://orcid.org/0000-0002-8879-2676
Pierre-Yves Blanchard https://orcid.org/0000-0003-1659-6868
Sara Cavaliere https://orcid.org/0000-0003-0939-108X
Bénédicte Prelot https://orcid.org/0000-0002-9478-6694

References

1. M. Luo and S. Guo, *Nat. Rev. Mater.*, **2**, 1 (2017).
2. G. Ercolano, S. Cavaliere, J. Rozière, and D. J. Jones, *Curr. Opin. Electrochem.*,, **9**, 271 (2018).
3. L. Du, Y. Shao, J. Sun, G. Yin, J. Liu, and Y. Wang, *Nano Energy*, **29**, 314 (2016).
4. C. Reiser, L. Bregoli, and T. Patterson, *Electrochem. Solid-State Lett.*, **8**, A273 (2005).
5. S. Shahgaldi and J. Hamelin, *Carbon N. Y.*, **94**, 705 (2015).
6. H. Liu, J. Li, X. Xu, F. Wang, J. Liu, Z. Li, and J. Ji, *Electrochim. Acta*, **93**, 25 (2013).
7. R. Balgis, G. M. Anilkumar, S. Sago, T. Ogi, and K. Okuyama, *J. Power Sources*, **203**, 26 (2012).
8. I. Savych, J. Bernard d'Arbigny, S. Subianto, S. Cavaliere, D. J. Jones, and J. Rozière, *J. Power Sources*, **257**, 147 (2014).
9. M. Ouattara-Brigaudet, S. Berthon-Fabry, C. Beauger, M. Chatenet, N. Job, M. Sennour, and P. Achard, *Int. J. Hydrogen Energy*, **37**, 9742 (2012).
10. T. Zhang, P. Wang, H. Chen, and P. Pei, *Appl. Energy*, **223**, 249 (2018).
11. T. Mittermeier, A. Weiß, F. Hasché, G. Hübner, and H. A. Gasteiger, *J. Electrochem. Soc.*, **164**, F127 (2017).
12. I. Jiménez-Morales, A. Reyes-Carmona, M. Dupont, S. Cavaliere, M. Rodlert, F. Mornaghini, M. J. Larsen, M. Odgaard, J. Zajac, D. J. Jones, and J. Rozière, *Carbon Energy*, **3**, 654 (2021).
13. Z. Lin, L. Ji, W. E. Krause, and X. Zhang, *J. Power Sources*, **195**, 5520 (2010).
14. Y. Luo, N. Shroti, M. K. Daletou, L. A. Estudillo-Wong, and N. Alonso-Vante, *J. Catal.*, **344**, 712 (2016).
15. A. Orfanidi, P. Madkikar, H. A. El-Sayed, G. S. Harzer, T. Kratky, and H. A. Gasteiger, *J. Electrochem. Soc.*, **164**, F418 (2017).
16. F. Forouzandeh, X. Li, D. W. Banham, F. Feng, A. Joseph Kakanat, S. Ye, and V. Birss, *J. Power Sources*, **378**, 732 (2018).
17. D. Liu, X. Zhang, Z. Sun, and T. You, *Nanoscale*, **5**, 9528 (2013).
18. H. Yang, Y. Ko, W. Lee, A. Züttel, and W. Kim, *Mater. Today Energy*, **13**, 374 (2019).
19. D. S. Yang, S. Chaudhari, K. P. Rajesh, and J. S. Yu, *ChemCatChem*, **6**, 1236 (2014).
20. K. K. R. Datta, V. V. Balasubramanian, K. Ariga, T. Mori, and A. Vinu, *Chemistry*, **17**, 3390 (2011).
21. D. C. Higgins, D. Meza, and Z. Chen, *J. Phys. Chem. C*, **114**, 21982 (2010).
22. Y. Qiu, J. Yin, H. Hou, J. Yu, and X. Zuo, *Electrochim. Acta*, **96**, 225 (2013).
23. J. Liang, Y. Jiao, M. Jaroniec, and S. Z. Qiao, *Angew. Chemie - Int. Ed.*, **51**, 11496 (2012).
24. Y. Chen, P. Xu, R. Wang, and X. Pan, *Mater. Lett.*, **286**, 129266 (2021).
25. H. G. Jo, K. H. Kim, and H. J. Ahn, *Appl. Surf. Sci.*, **554**, 149594 (2021).
26. Y. Zhou, K. Neyerlin, T. S. Olson, S. Pylypenko, J. Bult, H. N. Dinh, T. Gennett, Z. Shao, and R. O'Hayre, *Energy Environ. Sci.*, **3**, 1437 (2010).
27. V. Perazzolo, R. Brandiele, C. Durante, M. Zerbetto, V. Causin, G. A. Rizzi, I. Cerri, G. Granozzi, and A. Gennaro, *ACS Catal.*, **8**, 1122 (2018).
28. J. Liu, W. Li, R. Cheng, Q. Wu, J. Zhao, D. He, and S. Mu, *Langmuir*, **35**, 2580 (2019).
29. J. A. Prithi, N. Rajalakshmi, and G. Ranga, *Rao, Int. J. Hydrogen Energy*, **43**, 4716 (2018).
30. X. Wang, S. Yang, Y. Yu, M. Dou, Z. Zhang, and F. Wang, *Catal. Sci. Technol.*, **10**, 65 (2020).
31. R. Imran Jafri, N. Rajalakshmi, and S. Ramaprabhu, *J. Mater. Chem.*, **20**, 7114 (2010).
32. S. Zhang and S. Chen, *J. Power Sources*, **240**, 60 (2013).
33. H. Schmies, E. Hornberger, B. Anke, T. Jurzinsky, H. N. Nong, F. Dionigi, S. Kühl, J. Drnec, M. Lerch, C. Cremers, and P. Strasser, *Chem. Mater.*, **30**, 7287 (2018).
34. S. Woo, S. Lee, A. Z. Taning, T. H. Yang, S. H. Park, and S. D. Yim, *Curr. Opin. Electrochem.*, **21**, 289 (2020).
35. S. Ott, A. Orfanidi, H. Schmies, B. Anke, H. N. Nong, J. Hübner, U. Gernert, M. Gliech, M. Lerch, and P. Strasser, *Nat. Mater.*, **19**, 77 (2020).
36. Z. Fang, M. S. Lee, J. Y. Kim, J. H. Kim, and T. F. Fuller, *J. Electrochem. Soc.*, **167**, 064506 (2020).
37. Z. Yan, J. Xie, S. Zong, M. Zhang, Q. Sun, and M. Chen, *Electrochim. Acta*, **109**, 256 (2013).
38. H. Zhang, H. Wang, K. Jiao, and J. Xuan, *Appl. Energy*, **268**, 115053 (2020).
39. S. Yarova, D. Jones, F. Jaouen, and S. Cavaliere, *Surfaces*, **2**, 159 (2019).
40. K. Hyun, T. Ueno, O. L. Li, and N. Saito, *RSC Adv.*, **6**, 6990 (2016).
41. S. Dou, L. Tao, R. Wang, S. El Hankari, R. Chen, and S. Wang, *Adv. Mater.*, **30**, 1 (2018).
42. H. Liang, F. Ming, and H. N. Alshareef, *Adv. Energy Mater.*, **8**, 1 (2018).
43. K. Loganathan, D. Bose, and D. Weinkauf, *Int. J. Hydrogen Energy*, **39**, 15766 (2014).
44. M. Abrar, G. U. Farwa, S. Naseer, A. Saeed, A. W. Khan, Z. Iqbal, S. T. Hussain, and M. Zakaullah, *Curr. Appl Phys.*, **13**, 567 (2013).
45. Y. Shao, S. Zhang, M. H. Engelhard, G. Li, G. Shao, Y. Wang, J. Liu, I. a. Aksay, and Y. Lin, *J. Mater. Chem.*, **20**, 7491 (2010).
46. C. Zhang, J. Hu, X. Zhang, X. Wang, and Y. Meng, *Catal. Today*, **256**, 193 (2015).
47. G. Massaglia, A. Sacco, M. Castellino, A. Chiodoni, F. Frascella, S. Bianco, C. F. Pirri, and M. Quaglio, *Int. J. Hydrogen Energy*, **46**, 13845 (2021).
48. S. Kim, M. H. Cho, J. R. Lee, and S. J. Park, *J. Power Sources*, **159**, 46 (2006).
49. M. J. Larsen, I. Jiménez Morales, S. Cavaliere, J. Zajac, D. J. Jones, J. Rozière, L. Kaluža, D. Gulková, and M. Odgaard, *Int. J. Hydrogen Energy*, **42**, 7166 (2017).
50. T. Jawhari, A. Roid, and J. Casado, *Carbon N. Y.*, **33**, 1561 (1995).
51. N. Satyanarayana, C. S. Bhatia, S. Tripathy, S. Kundu, N. Dwivedi, and R. J. Yeo, *Sci Rep.*, **5**, 1 (2015).
52. S. Brunauer, P. H. Emmett, and E. Teller, *J. Am. Chem. Soc.*, **60**, 309 (1938).
53. J. Jagiello and J. P. Olivier, *Adsorption*, **19**, 777 (2013).
54. M. Rybin, A. Pereyaslavtsev, T. Vasilieva, V. Myasnikov, I. Sokolov, A. Pavlova, E. Obraztsova, A. Khomich, V. Ralchenko, and E. Obraztsova, *Carbon N. Y.*, **96**, 196 (2016).
55. T. Susi, T. Pichler, and P. Ayala, *Beilstein J. Nanotechnol.*, **6**, 177 (2015).
56. L. G. Caṇado, K. Takai, T. Enoki, M. Endo, Y. A. Kim, H. Mizusaki, A. Jorio, L. N. Coelho, R. Magalhães-Paniago, and M. A. Pimenta, *Appl. Phys. Lett.*, **88**, 2 (2006).
57. O. Baranov, I. Levchenko, J. M. Bell, J. W. M. Lim, S. Huang, L. Xu, B. Wang, D. U. B. Aussems, S. Xu, and K. Bazaka, *Mater. Horizons*, **5**, 765 (2018).
58. M. R. Buchmeiser, J. Unold, K. Schneider, E. B. Anderson, F. Hermanutz, E. Frank, A. Müller, and S. Zinn, *J. Mater. Chem. A*, **1**, 13154 (2013).
59. M. Thoma, W. Lin, E. Hoffmann, M. M. Sattes, D. Segets, C. Damm, and W. Peukert, *Langmuir*, **34**, 12324 (2018).
60. S. M. Andersen, M. Borghei, R. Dhiman, V. Ruiz, E. Kauppinen, and E. Skou, *J. Phys. Chem. C*, **118**, 10814 (2014).
61. C. M. González-García, M. L. González-Martín, R. Denoyel, A. M. Gallardo-Moreno, L. Labajos-Broncano, and J. M. Bruque, *Carbon N. Y.*, **43**, 567 (2005).
62. Z. Király, G. H. Findenegg, E. Klumpp, H. Schlimper, and I. Dékány, *Langmuir*, **17**, 2420 (2001).
63. I. Jiménez-Morales, S. Cavaliere, D. Jones, and J. Rozière, *Phys. Chem. Chem. Phys.*, **20**, 8765 (2018).
64. F. Raynal, A. Etcheberry, S. Cavaliere, V. Noël, and H. Perez, *Appl. Surf. Sci.*, **252**, 2422 (2006).
65. P. Q. Phan, R. Naraprawatphong, P. Pornaroontham, J. Park, C. Chokradjaroen, and N. Saito, *Mater. Adv.*, **2**, 322 (2021).
66. E. G. Ciapina, S. F. Santos, and E. R. Gonzalez, *J. Electroanal. Chem.*, **815**, 47 (2018).
67. K. Kinoshita, *J. Electrochem. Soc.*, **137**, 845 (1990).
68. F. Maillard, S. Schreier, M. Hanzlik, E. R. Savinova, S. Weinkauf, and U. Stimming, *Phys. Chem. Chem. Phys.*, **7**, 375 (2005).
69. S. Taylor, E. Fabbri, P. Levecque, T. J. Schmidt, and O. Conrad, *Electrocatalysis*, **7**, 287 (2016).